

Orbital torque switching of room temperature two-dimensional van der Waals ferromagnet Fe_3GaTe_2

Received: 20 November 2024

Accepted: 18 July 2025

Published online: 31 July 2025

 Check for updates

Delin Zhang  , Heshuang Wei^{1,7}, Jinyu Duan^{1,7}, Jiali Chen ,
Jiaxin Chen⁵, Dongdong Yue⁶, Wanxi Gong⁵, Pengfei Liu¹, Yuhe Yang²,
Jinlong Gou¹, Junxin Yan⁶, Kun Zhai , Ping Wang¹, Shuai Hu¹, Zhiyan Jia²,
Wei Jiang , Liang Liu , Wenhong Wang , Yue Li  &
Yong Jiang , 

Efficiently manipulating the magnetization of van der Waals (vdW) ferromagnets has attracted considerable interest in developing room-temperature two-dimensional (2D) material-based memory and logic devices. Here, taking advantage of the unique properties of the vdW ferromagnet as well as promising characteristics of the orbital Hall effect, we demonstrate the room-temperature magnetization switching of vdW ferromagnet Fe_3GaTe_2 through the orbital torque generated by the orbital Hall material, Titanium (Ti). The switching current density is estimated to be around $1.6 \times 10^6 \text{ A/cm}^2$, comparable to that achieved in Fe_3GaTe_2 using spin-orbit torque from spin Hall materials (e.g., WTe_2 , and TlIrTe_4). The efficient magnetization switching arises from the combined effects of the large orbital Hall conductivity of Ti and the strong spin-orbit correlation of the Fe_3GaTe_2 , as confirmed through theoretical calculations. Our findings advance the understanding of orbital torque switching and pave the way for exploring 2D material-based orbitronic devices.

Spintronic devices have been extensively studied for their potential in developing energy-efficient memory and computing components, offering ultrahigh storage density, ultrafast switching speed, ultralow energy consumption, and excellent scalability^{1–3}. These devices are primarily manipulated through spin-transfer torque (STT), where the charge current (I_C) can be converted into spin current (I_S) via the ferromagnets with high spin polarization⁴, or by spin-orbit torque (SOT), where the conversion happens through spin Hall materials (SHMs) with strong spin-orbit coupling (SOC)^{5–7}. Despite significant

advancements over the past decade, spintronic memory devices still face several challenges. STT-based memory devices struggle with relatively low endurance, high switching current density, and Joule heating caused by the current flowing through the tunnel barrier. SOT-based devices require SHMs with strong SOC for efficient spin-torque generation. Recently, attention has increasingly shifted toward orbitronic devices, where device manipulation is driven by orbital torque (OT) generated by the orbital Hall effect (OHE) through an orbital Hall material (OHM) with the weak SOC^{8–22}. This approach

¹Institute of Quantum Materials and Devices; School of Electronics and Information Engineering, Tiangong University, Tianjin, China. ²School of Material Science and Engineering; State Key Laboratory of Advanced Separation Membrane Materials, Tiangong University, Tianjin, China. ³School of Physical Science & Technology, Tiangong University, Tianjin, China. ⁴Centre for Quantum Physics, Key Laboratory of Advanced Optoelectronic Quantum Architecture and Measurement (MOE); Beijing Key Lab of Nanophotonics & Ultrafine Optoelectronic Systems, School of Physics, Beijing Institute of Technology, Beijing, China.

⁵Tsung-Dao Lee Institute, Key Laboratory of Artificial Structures and Quantum Control (Ministry of Education), School of Physics and Astronomy, Shanghai Jiao Tong University, Shanghai, China. ⁶Center for High Pressure Science, State Key Laboratory of Metastable Materials Science and Technology, Yanshan University, Qinhuangdao, China. ⁷These authors contributed equally: Delin Zhang, Heshuang Wei, Jinyu Duan, Jiali Chen.

 e-mail: zhangdelin@tiangong.edu.cn; wjiang@bit.edu.cn; yjiang@tiangong.edu.cn

has the potential to overcome the challenges faced by spintronic devices.

The OHE originates from the orbital texture created by the orbital hybridization, which generates finite orbital angular momentum along the direction of $\mathbf{E} \times \mathbf{k}$ under an external electric field (\mathbf{E})^{8–10}. Unlike STT⁴ and SOT devices, which rely solely on charge-to-spin conversion^{5–7}, OT devices involve two stages of current conversion: the J_C -to-orbital current (J_L) conversion in the OHM and the J_L -to- J_S conversion in the adjacent ferromagnetic (FM) material. This unique mechanism allows for tuning the OT efficiency (ξ_{OT}) by designing novel heterostructures with optimal selections of OHM and FM material combinations²⁰. So far, many OHMs have been predicted to efficiently convert J_C to J_L due to their giant orbital Hall conductivity (σ_{OHE})^{9,11,16}. For example, experiments have shown these materials have a large ξ_{OT} (-0.78)²⁰ and a long orbital diffusion length (λ_{OHE}) (-60 nm)¹⁶. However, the options for FM materials capable of efficiently converting J_L to J_S are limited, particularly for perpendicular magnetic anisotropy (PMA) materials with a strong spin-orbit correlation^{15,20,23}. Therefore, exploring novel PMA FM materials is crucial for advancing orbitronic devices.

Recent advancements in two-dimensional van der Waals (2D-vdW) materials have led to the experimental confirmation of various 2D-vdW FM materials, opening new avenues for innovative room-temperature 2D-vdW spintronic technologies^{24–27}. Among these advancements, 2D-vdW Fe_3GaTe_2 has emerged as a particularly promising FM material, drawing considerable attention for its potential applications in tunnel magnetoresistance^{28,29}, magnetic skyrmions^{30–33}, and SOT devices^{34–39}. This interest is driven by its clean surface, large PMA ($K_u > 3.88 \times 10^5 \text{ J/m}^3$), and high Curie temperature ($T_c > 350 \text{ K}$)⁴⁰. Notably, SOT-driven magnetization switching in Fe_3GaTe_2 -based heterostructures has been experimentally demonstrated using SHMs with large SOC, such as heavy metals^{34–36}, topological insulators³⁷, and topological semimetals^{38,39}. However, the OT-driven magnetization switching of the Fe_3GaTe_2 material has yet to be observed, and the underlying switching mechanism for 2D-vdW ferromagnets remains elusive.

In this work, we experimentally investigated the OT-driven magnetization switching of the 2D-vdW ferromagnet Fe_3GaTe_2 through the Ti OHM and provided a theoretical and experimental understanding of the OT-driven magnetization switching mechanism. The relatively large ξ_{OT} of Ti OHM is first obtained in the Ti/Ni heterostructures through the spin-torque ferromagnetic resonance (ST-FMR), suggesting the strong OHE of the Ti OHM. Then the Fe_3GaTe_2 -based heterostructures were fabricated and patterned into Hall bar devices, followed by the harmonic Hall voltage measurement and current-induced magnetization switching. We obtained the larger damping-like torque (ξ_{DL} ~ 0.26) and realized the magnetization switching of the Fe_3GaTe_2 layer at room temperature in the $\text{Fe}_3\text{GaTe}_2/\text{Ti}$ device with a significantly lower switching current density ($J_{\text{switching}}$) ~ $1.6 \times 10^6 \text{ A/cm}^2$. Meanwhile, first-principles calculations were employed to analyze the spin-orbit correlation in Fe_3GaTe_2 structures, shedding light on the underlying mechanism of OT-driven magnetization switching of 2D-vdW FM materials. These findings highlight the significance of spin-orbit correlation in the PMA FM materials, providing valuable insights for the design and development of 2D-vdW orbitronic devices.

Results

Orbital torque device based on 2D-vdW ferromagnet

In 2D-vdW FM SOT heterostructures, the J_S can be generated by SHMs [e.g., $\text{Pt}^{34–36}$, $\text{Bi}_{1.1}\text{Sb}_{0.9}\text{Te}_2\text{S}^{37}$, and WTe_2^{39}], and then these J_S flow into 2D-vdW ferromagnets, exerting a torque that switches their magnetization. The efficiency of the magnetization switching mainly depends on the spin Hall angle (θ_{SHE}) of the SHMs. However, in 2D-vdW FM OT heterostructures, the switching efficiency depends not only on the orbital Hall angle (θ_{OHE}) of the OHMs but also on the orbital-to-spin conversion coefficient (η_{L-S}) of the 2D-vdW ferromagnets. OHMs with

high σ_{OHE} convert J_C into J_L via the OHE. The J_L then flows into the adjacent 2D-vdW FM layer, where it is converted into J_S through strong spin-orbit correlation, generating the torque to switch the magnetization of the 2D-vdW FM layer, as shown in the left panel of Fig. 1a. Therefore, both OHMs with high σ_{OHE} and 2D-vdW FM materials with strong spin-orbit correlation are essential for enhancing the ξ_{OT} .

Here, we selected Ti as the OHM and the 2D-vdW Fe_3GaTe_2 as the PMA FM layer to investigate the J_C -to- J_L -to- J_S conversion and the OT-driven magnetization switching. The J_C can be efficiently converted into the J_L through the Ti OHM, which has a larger σ_{OHE} , calculated to be approximately $4600 (\text{h/e})(\text{S/cm})$. It is worth noting that, due to its weak SOC, Ti exhibits a negligible spin Hall conductivity (σ_{SHE}) of only about $11 (\text{h/e})(\text{S/cm})$, effectively ruling out the possibility of any significant SOT effect, as shown in Fig. 1b¹⁶. The J_L generated in the Ti OHM layer can be efficiently converted into J_S due to the strong SOC of the Fe_3GaTe_2 layer (see the right panel of Fig. 1a).

The Fe_3GaTe_2 possesses the hexagonal structure with two adjacent quintuple-layered substructures separated by a vdW gap, where each quintuple layer consists of a Fe_3Ga heterometallic slab sandwiched between two Te layers, as illustrated in Fig. 1a. Fe_3GaTe_2 single crystal samples, grown by the self-flux method, exhibit high-quality crystallinity, as demonstrated by prominent $(00L)$ Bragg peaks (see Supplementary Fig. 1a) with an estimated Curie temperature of $\sim 365 \text{ K}$ (see Supplementary Fig. 1b and Supplementary Note 1 for more details). Fig. 1c presents the microstructure of the $\text{Fe}_3\text{GaTe}_2/\text{Ti}$ (10.0 nm) heterostructure measured by the atomic-resolution scanning transmission electron microscopy (STEM). The crystalline structure of the layered Fe_3GaTe_2 and the high-quality interface of $\text{Fe}_3\text{GaTe}_2/\text{Ti}$ are confirmed in the representative cross-sectional high-angle annular dark field STEM (HAADF-STEM) image of the $\text{Fe}_3\text{GaTe}_2/\text{Ti}$ device. As shown in Fig. 1c, each layer of Fe_3GaTe_2 is constituted by the alternately arranged Te-Fe-Ga(Fe)-Fe-Te atomic planes. A polycrystalline Ti layer is uniformly sputtered on the Fe_3GaTe_2 layer, and the interface of $\text{Fe}_3\text{GaTe}_2/\text{Ti}$ is flat and clean. Furthermore, through the corresponding X-ray energy dispersive spectrometry (EDS) map of the Fe, Ga, Te, and Ti elements, we observed the presence of sharp interfaces, indicating there is no obvious intermigration between the Fe_3GaTe_2 and Ti layers.

Orbital torque efficiency

To investigate the ξ_{OT} of the Ti OHM, the Ti (7–40 nm)/Ni (5 nm) samples were prepared and patterned into the devices with the size of $20 \mu\text{m} \times 45 \mu\text{m}$. Then the ξ_{OT} was measured by the ST-FMR methods (see details in Supplementary Note 2). In the ST-FMR measurements, the oscillatory resistance leads to a rectified mixing voltage (V_{mix}) due to magnetization precession coherent with the RF current⁴¹. V_{mix} is composed of V_S and V_A parts, where V_S and V_A represent the amplitudes of the symmetric and antisymmetric components which are proportional to the in-plane damping-like torque and out-of-plane torques, respectively. To exclude possible parasitic effects, the angular dependence of V_S and V_A is measured by sweeping in-plane external magnetic field (H_{ext}) along with different directions (θ)⁴¹. The ξ_{OT} can be expressed as $\xi_{OT} = (V_S^0/V_A^0)(\frac{e\mu_0 M_{\text{eff}} t d}{\hbar})[1 + (4\pi M_{\text{eff}}/H_{\text{ext}})]^{1/2}$, where \hbar is the reduced Planck's constant, μ_0 is the permeability of free space, M_{S} is the saturation magnetization, t is the thickness of the Ni layer, d is the thickness of the Ti OHM layer, and M_{eff} is the effective magnetization of the Ti/Ni bilayer. Fig. 2a, b and Supplementary Fig. 2 show the V_{mix} vs. H_{ext} and angular dependence of V_S and V_A for the Ti (7–40 nm)/Ni (5 nm) devices. Through fitting raw data, the ξ_{OT} is estimated to be 0.05–0.28 with an increase in the thickness of the Ti layer from 7 nm to 40 nm. These results demonstrate the dominant bulk OHE contribution from the Ti OHM layer in the $\text{Fe}_3\text{GaTe}_2/\text{Ti}$ heterostructure. However, the interfacial orbital Rashba-Edelstein effect (OREE) contribution arising from symmetry breaking at the $\text{Fe}_3\text{GaTe}_2/\text{Ti}$ interface cannot be entirely excluded due to experimental limitations in

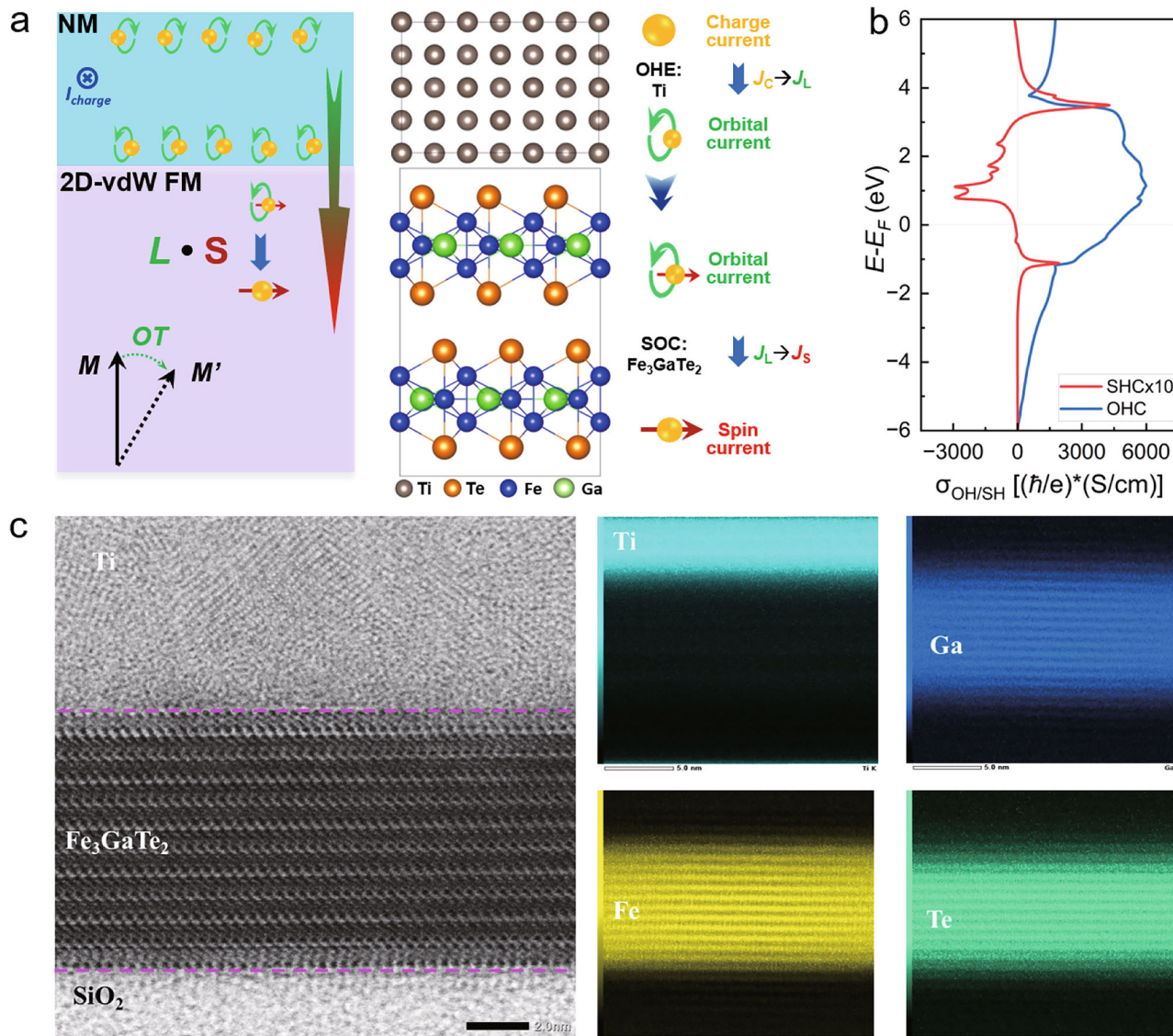


Fig. 1 | Orbital torque in van der Waals ferromagnet. **a** Schematic of the $\text{Fe}_3\text{GaTe}_2/\text{Ti}$ orbital torque heterostructure, in which the Ti orbital Hall material converts the charge current (J_c) into the orbital current (J_L), then the orbital current (J_L) flows into the 2D-vdW FM Fe_3GaTe_2 layer and is converted into the spin current (J_S) due to the spin-orbit coupling of the Fe_3GaTe_2 layer. **b** The calculated

orbital Hall conductivity (blue line) and spin Hall conductivity (red line) of the Ti orbital Hall material. **c** The microstructure of the $\text{Fe}_3\text{GaTe}_2/\text{Ti}$ heterostructure measured by the atomic-resolution scanning transmission electron microscopy (STEM).

resolving opposing Oersted and field-like effect fields, which warrants further investigations.

To understand the physical mechanism of the magnetization switching, we fabricated the Fe_3GaTe_2 (-15 nm)/ Ti (10 nm) devices, and then quantitatively characterized damping-like effective field (H_{DLy}) and field-like effective field (H_{FLy}) through the harmonic Hall voltage measurement (see details in Supplementary Note 2)^{36,42}. When an alternating current is applied to the device, the OT drives magnetization oscillations at the frequency of the alternating current. Due to the nonlinear nature of the system, these oscillations generate a second harmonic Hall resistance $R_{xy}^{2\omega}$, described as:

$$R_{xy}^{2\omega} = \left(R_{\text{AHE}} \frac{H_{\text{DLy}}}{H_{\text{ext}} + H_{\text{dem}} - H_k} + R_{\text{Ther}} \right) \cos \varphi + \left(2R_{\text{PHE}} \frac{H_{\text{FLy}} + H_{\text{Oe}}}{H_{\text{ext}}} \right) \cos(2\varphi) \cos \varphi$$

where R_{AHE} , R_{PHE} , R_{Ther} , H_{DLy} , H_{FLy} , H_{ext} , H_{dem} , and H_k are anomalous Hall resistance, planar Hall resistance, resistance of thermal contributions from spin Seebeck effect, and anomalous Nernst effect, damping-

like effective field, field-like effective field, external magnetic field, demagnetization field, and anisotropy field, respectively. For simplicity, the coefficients of $\cos \varphi$ and $\cos(2\varphi) \cos \varphi$ terms are denoted as A and B , respectively, where $A = R_{\text{AHE}} \frac{H_{\text{DLy}}}{H_{\text{eff}}} + R_{\text{Ther}}$, $B = 2R_{\text{PHE}} \frac{H_{\text{FLy}} + H_{\text{Oe}}}{H_{\text{ext}}}$, and $H_{\text{eff}} = H_{\text{ext}} + H_{\text{dem}} - H_k$. Fig. 2c shows $R_{xy}^{2\omega}$ versus the azimuth angle φ under $H_{\text{ext}} = 4.5$ T. By fitting the $R_{xy}^{2\omega} - \varphi$ relations under different H_{ext} , we can obtain the $1/H_{\text{eff}}$ dependence of A and the $1/H_{\text{ext}}$ dependence of B , as shown in Fig. 2d and Supplementary Fig. 3d, respectively. By fitting A and B , we can obtain H_{DLy} and H_{FLy} of the Fe_3GaTe_2 (-15 nm)/ Ti (10 nm) device. The corresponding damping-like torque efficiency ξ_{DL} is estimated to be -0.26 following the equation of $\xi_{\text{DL}} = \frac{(2e)}{\hbar} M_s t_{\text{FM}} \frac{\mu_0 H_{\text{DLy}}}{J_{\text{Ti}}}$, where M_s , t_{FM} , and J_{Ti} represent the magnetization, thickness of the Fe_3GaTe_2 layer, and the applied current density of the Ti layer, respectively. For the field-like torque ξ_{FL} , an accurate H_{FLy} cannot be well fitted because R_{PHE} is quite small (~10 mΩ) for our device. Thus, the ξ_{FL} is roughly estimated to be around -0.06. These results reveal

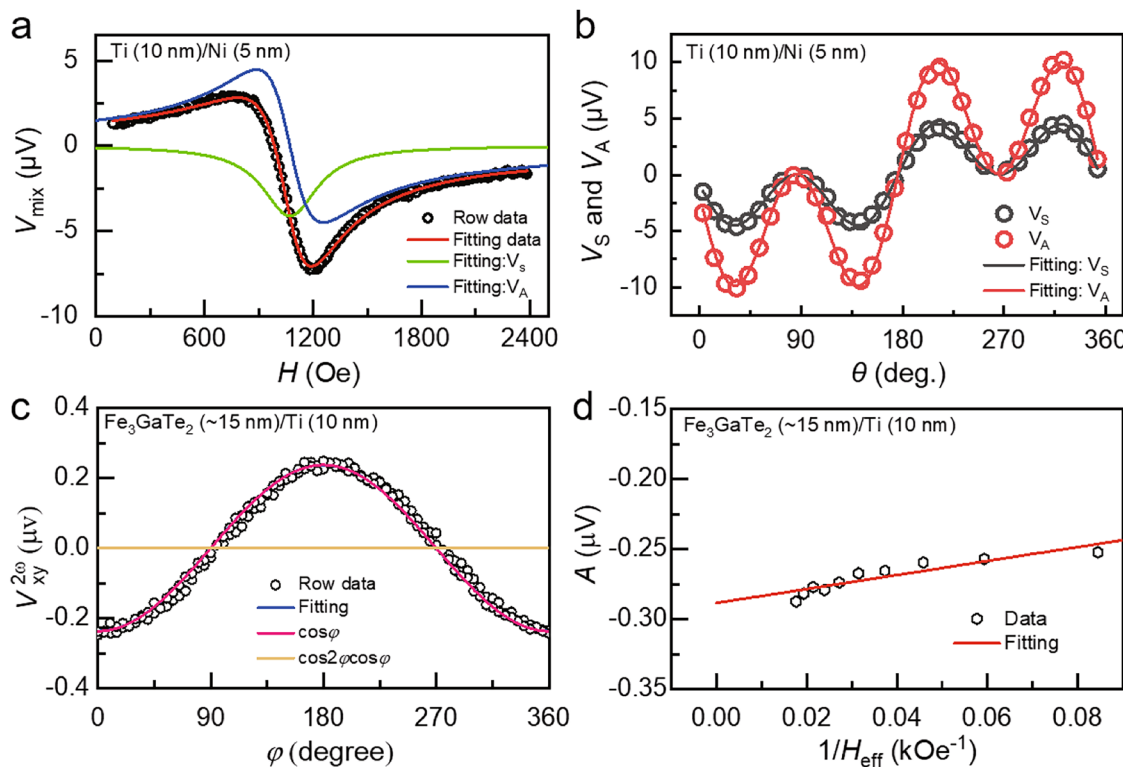


Fig. 2 | Orbital torque efficiency. **a** The V_{mix} and the corresponding fitting V_A and V_S of the Ti (10 nm)/Ni (5 nm) device were measured by the spin-torque ferromagnetic resonance method under 8.5 GHz. **b** Angular dependence of V_A and V_S and the corresponding $\sin 2\phi \cos \phi$ fittings for Ti (10 nm)/Ni (5 nm) device.

c Azimuthal angle (ϕ) dependent second harmonic Hall resistance $R_{xy}^{2\omega}$ under $H_{\text{ext}} = 4.5$ T of the Fe₃GaTe₂ (~15 nm)/Ti (10 nm) device measured by the harmonic Hall voltage measurement method. **d** The A value as a function of the $1/H_{\text{eff}}$ by fitting $V_{xy}^{2\omega} - \phi$ relations under different H_{ext} .

that both the ξ_{DL} and ξ_{FL} contribute to the magnetization switching, but the ξ_{DL} plays the dominant role. Therefore, it is likely that the J_L generated in the Ti layer via the OHE is converted into the J_S in the Fe₃GaTe₂ layer. Moreover, the J_L can also exert a direct OT without the J_L -to- J_S conversion, governed jointly by the SOC and magnetic exchange coupling. This direct OT may exhibit long-range characteristics due to the crystal-field splitting induced orbital transport “hotspots” in momentum space^{15,43}, which facilitate extended J_L propagation. Both mechanisms are consistent with the observed dominance of damping-like torque, as they ultimately generate spin-polarized currents or orbital-derived effective fields that drive coherent magnetization rotation.

Orbital torque switching of 2D-vdW ferromagnet

To experimentally investigate the OT-driven magnetization switching, we fabricated the 2D-vdW FM Fe₃GaTe₂/Ti samples on the Si/SiO₂ substrates, which were patterned into Hall bar devices (15 μm × 6 μm) (see the inset of Fig. 3a and Supplementary Fig. 4a) and characterized for current-induced magnetization switching through the OT (see the device fabrication and transport-property measurements in Methods). To assess the PMA of the Fe₃GaTe₂ (15.8 nm)/Ti (10.0 nm) Hall bar device, the room-temperature anomalous Hall resistance (R_{xy}) vs. H_{ext} loop was measured with both the in-plane and out-of-plane H_{ext} , as shown in Fig. 3a and Supplementary Fig. 4b. The effective anisotropy fields (H_K) were estimated to be 4.02–5.33 T as the temperature decreased from 300 K to 225 K, verifying a very strong PMA^{36,38,39}. Meanwhile, the R_{xy} vs. out-of-plane H_{ext} loops at even lower temperatures were measured to further characterize the PMA, as plotted in Fig. 3b. The Hall bar device demonstrates 100% remanence with well-defined rectangle R_{xy} vs. H_{ext} loops. The coercivity (H_C) of the Fe₃GaTe₂ (15.8 nm)/Ti (10.0 nm) Hall bar device increases from 19 mT at 300 K to 540 mT at 10 K, indicating very strong PMA. In addition, as the device

was cooled from 300 K to 200 K, the value of R_{xy} increases from 4.7 Ω to 7.7 Ω, as plotted in Fig. 3c, suggesting the excellent magnetic properties of the 2D-vdW Fe₃GaTe₂ layer. In addition, there could be also a potential self-induced spin-orbit torque from Fe₃GaTe₂ that helps the magnetization switching. To check this point, we theoretically calculated the σ_{SHC} and experimentally investigated the magnetization switching of Fe₃GaTe₂. The results are shown in Supplementary Fig. 5. It is found that σ_{SHC} is calculated to be around 69, 95, 116, and 130 (\hbar/e)(S/cm) for the monolayer, bilayer, trilayer, and bulk structures of Fe₃GaTe₂, respectively, which has negligible contribution compared to the σ_{OHC} of Ti [-4600 (\hbar/e)(S/cm)] (see Supplementary Fig. 5a). Meanwhile, the magnetization switching of the single Fe₃GaTe₂ layer was not observed, as presented in Supplementary Fig. 5b. Therefore, the magnetization switching for the Fe₃GaTe₂/Ti device is primarily influenced by both the OT of the Ti OHE ($\sigma_{\text{OHE,Ti}}$) and the spin-orbital correlation strength of the Fe₃GaTe₂ layer.

To demonstrate the OT-driven magnetization switching of the 2D-vdW FM Fe₃GaTe₂ layer, the R_{xy} vs. the pulse current (I_{pulse}) loops of the Fe₃GaTe₂ (15.8 nm)/Ti (10.0 nm) Hall bar device were measured by applying the I_{pulse} with 1 ms write-pulse and a 6 s delay followed by read pulses (± 1.0 mA) under in-plane $H_{\text{ext}} - \pm 20$ mT - ± 150 mT applied along the current direction (see details in Supplementary Note 3). The experimental results are shown in Fig. 3d and Supplementary Figs. 6–8. Although the Curie temperature of the Fe₃GaTe₂ single-crystal sample is around 365 K (see Supplementary Fig. 1b), it will be slightly lower for the 2D-vdW FM Fe₃GaTe₂ thin film³⁶. In this case, the PMA of the Fe₃GaTe₂ thin film can be easily decreased when the I_{pulse} is applied during the measurement of current-induced magnetization switching. Consequently, R_{xy} vs. I_{pulse} measurements were carried out at 300 K, 275 K, 250 K, and 225 K to ensure the FM state of Fe₃GaTe₂ with good PMA while studying the temperature-dependent magnetization switching behavior. Fig. 3d presents the R_{xy} vs. I_{pulse} loops of the

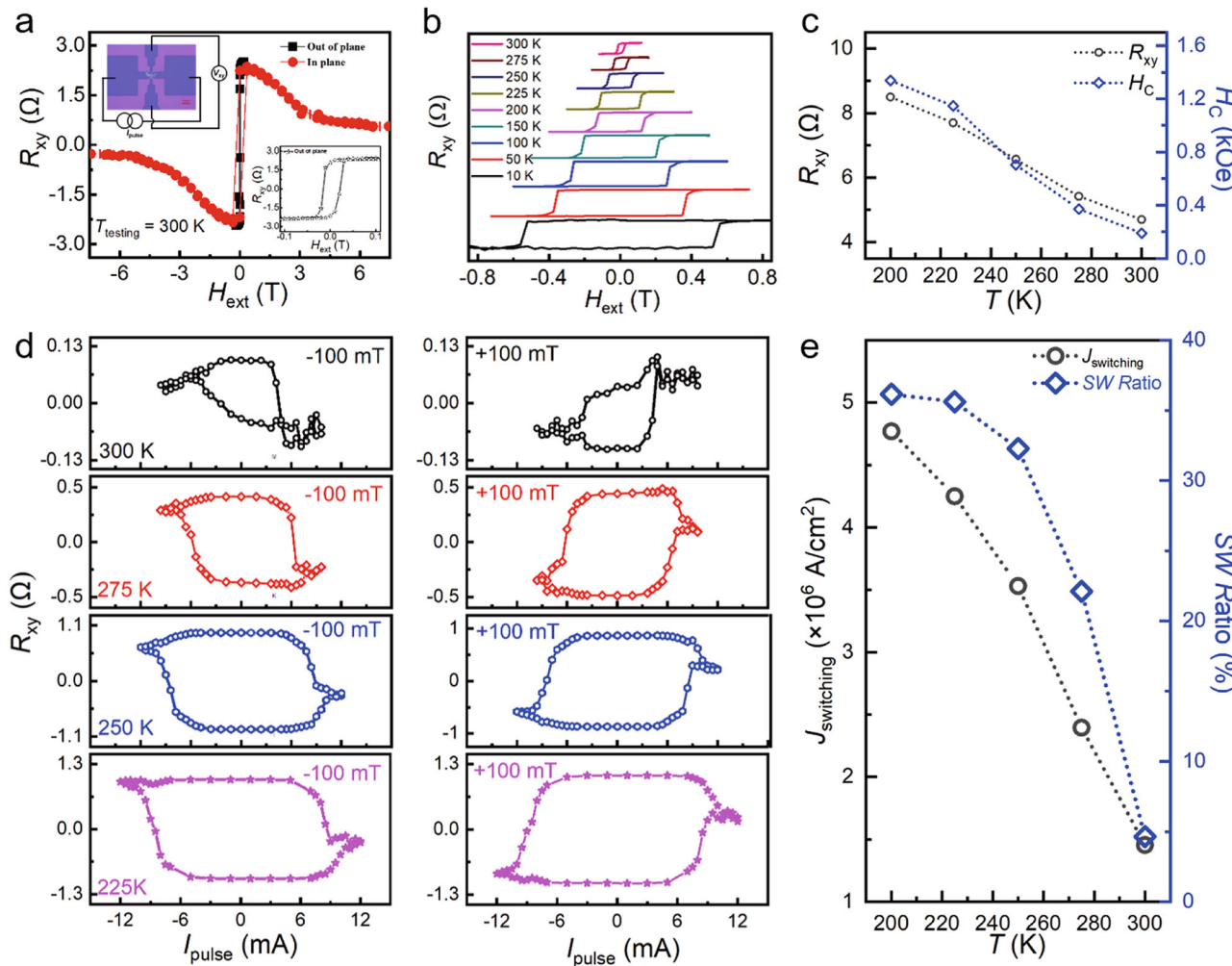


Fig. 3 | Orbital torque switching of 2D vdW ferromagnet. **a** The anomalous Hall resistance (R_{xy}) vs. the external magnetic field (H_{ext}) loops measured at room temperature of the 2D-vdW $\text{Fe}_3\text{GaTe}_2/\text{Ti}$ Hall bar device, where the H_{ext} is applied along in-plane and out-of-plane directions. The insets show the image of the Hall bar device and the zoom-in out-of-plane R_{xy} vs. H_{ext} loop. **b** The R_{xy} vs. out-of-plane H_{ext} loops as a function of measuring temperatures of the $\text{Fe}_3\text{GaTe}_2/\text{Ti}$ device. **c** The

curves of the R_{xy} vs. $T_{testing}$ and the coercivity (H_C) vs. $T_{testing}$ of the $\text{Fe}_3\text{GaTe}_2/\text{Ti}$ Hall bar device. **d** The R_{xy} vs. the pulse current (I_{pulse}) loops of the $\text{Fe}_3\text{GaTe}_2/\text{Ti}$ device measured with the in-plane $H_{ext} = \pm 100$ mT along the current direction at temperatures from 300 K to 225 K with the testing connection of $I^+ - V^+ - I^- - V^-$ along the clockwise direction. **e** The $J_{switching}$ vs. T and the switching ratio (SW Ratio) vs. T of the $\text{Fe}_3\text{GaTe}_2/\text{Ti}$ device.

Fe_3GaTe_2 (15.8 nm)/Ti (10.0 nm) Hall bar device measured with temperatures from 300 K to 225 K in the presence of a ± 100 mT in-plane H_{ext} . The low resistance and high resistance states were observed at the measured temperatures when switching the I_{pulse} from positive to negative polarities. Reversing the direction of the in-plane H_{ext} also resulted in a reversal of the polarity in the R_{xy} vs. I_{pulse} loops. Meanwhile, the ratio of magnetization switching exhibited an initial increase followed by a decrease as the in-plane H_{ext} increased, as shown in Supplementary Figs. 6–8. This behavior excludes thermal effects and confirms that the 180° magnetization switching is driven by the OT from the Ti OHM. In addition, the R_{xy} vs. I_{pulse} loops of the Fe_3GaTe_2 (15.8 nm)/Ti (10.0 nm) Hall bar device become rectangle (see Fig. 3c) as the measured temperature decreased from 300 K to 225 K, suggesting the deterministic magnetization switching. Fig. 3e shows the $J_{switching}$ and switching ratio as functions of temperature for the Fe_3GaTe_2 (15.8 nm)/Ti (10.0 nm) Hall bar device. It can be observed that the $J_{switching}$ gradually increases from 1.6×10^6 A/cm 2 to 4.8×10^6 A/cm 2 as the temperature decreases, attributed to the enhanced magnetic properties (e.g. PMA) of the Fe_3GaTe_2 layer as the temperature decreases. Notably, we observed that the switching ratio also increases as the devices are cooled. This enhancement may be attributed to the

reduced thermal perturbation and the enhanced PMA of the Fe_3GaTe_2 layer at lower temperatures. The suppression of thermal fluctuations stabilizes a single-domain state, while enhanced magnetic exchange coupling promotes coherent magnetization alignment³⁴. This enhancement may lead to an increase in direct OT generation governed jointly by the SOC and magnetic exchange coupling.

Orbital torque vs. spin-orbit torque

To further investigate the torque efficiency of OT, SOT, and the combined SOT + OT, we designed and prepared two additional samples: the SOT sample Fe_3GaTe_2 (18.3 nm)/Pt (5.0 nm) and the SOT + OT sample Fe_3GaTe_2 (16.7 nm)/Pt (2.0 nm)/Ti (10.0 nm). These samples were then patterned into the Hall bar devices ($24 \mu\text{m} \times 8 \mu\text{m}$), all of which exhibit excellent PMA properties, as evidenced by their square R_{xy} vs. H_{ext} loops. Subsequently, current-induced orbital/spin torque magnetization switching was performed under an in-plane H_{ext} applied along the current direction (see Fig. 4, Supplementary Note 3, and Supplementary Figs. 9–12). Unlike the squared R_{xy} vs. H_{ext} loops, the R_{xy} vs. the applied current density J loops do not always exhibit a perfectly squared signal measured at room temperature due to the thermal effect which resulted in magnetic moment disarrangement and PMA decrease. To ensure a

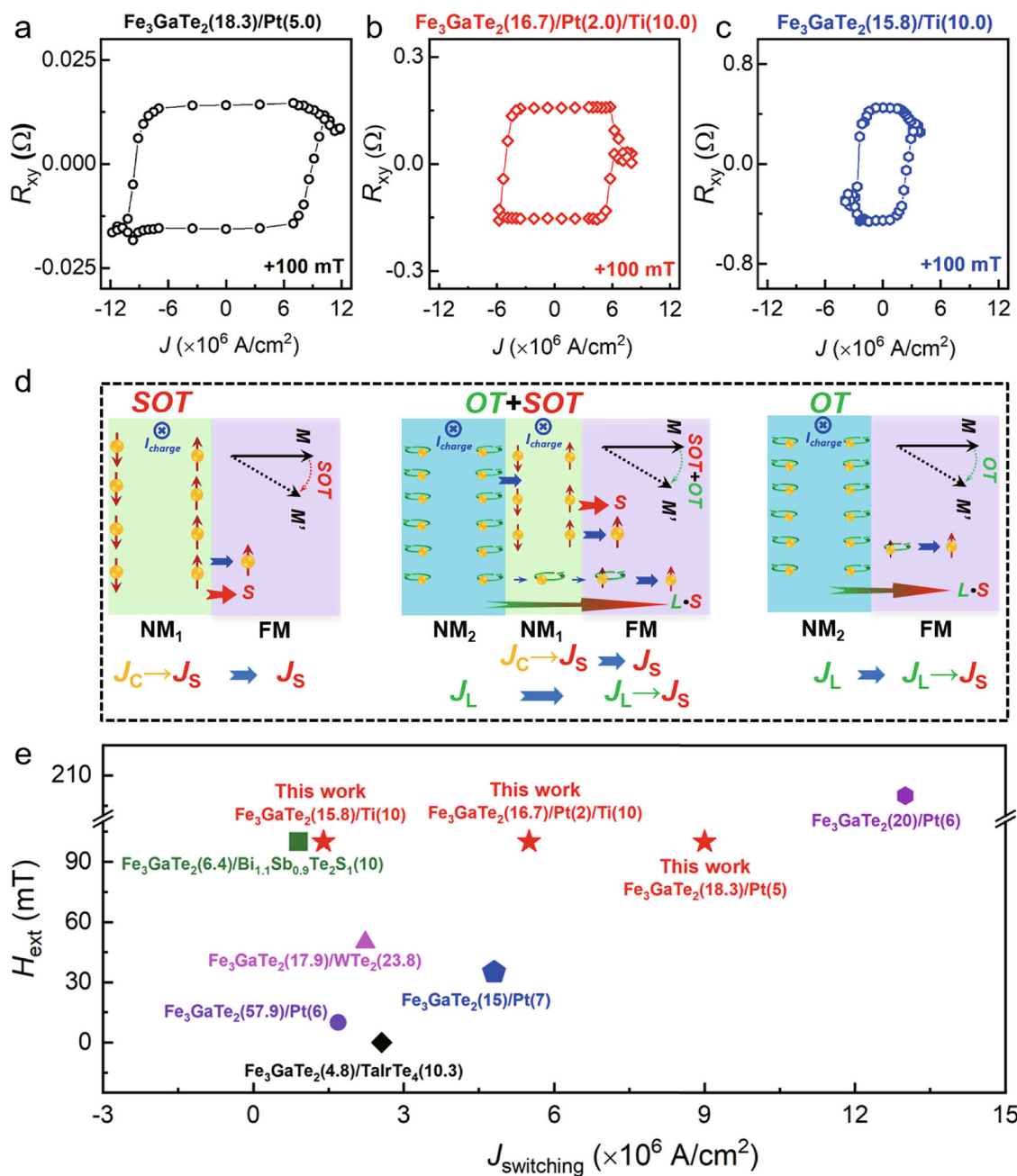


Fig. 4 | Orbital torque vs. Spin-orbit torque. **a–c** The anomalous Hall resistance (R_{xy}) vs. the applied current density (J) loops measured at 275 K of the 2D-vdW $\text{Fe}_3\text{GaTe}_2/\text{Pt}$, $\text{Fe}_3\text{GaTe}_2/\text{Pt}/\text{Ti}$, and $\text{Fe}_3\text{GaTe}_2/\text{Ti}$ Hall bar devices, respectively, under the in-plane external magnetic field (H_{ext}) = 100 mT along the current direction, where the testing connection is $I^+ - V^- - I^- - V^+$ for the $\text{Fe}_3\text{GaTe}_2/\text{Pt}$ device and

$I^+ - V^+ - I^- - V^-$ for $\text{Fe}_3\text{GaTe}_2/\text{Pt}/\text{Ti}$ and $\text{Fe}_3\text{GaTe}_2/\text{Ti}$ devices along the clockwise direction. **d** The physical mechanisms of the current conversion for the SOT, SOT + OT, and OT devices. **e** The summarized $J_{switching}$ values as a function of the in-plane H_{ext} for 2D-vdW Fe_3GaTe_2 heterostructures driven through the SOT and OT at room temperature.

fair comparison between different devices, we selected the R_{xy} vs. J loops measured at 275 K under an in-plane H_{ext} = 100 mT, where all devices display near square-shaped R_{xy} vs. J loops. We note that the slight variation in Fe_3GaTe_2 thickness across different devices does not significantly affect $J_{switching}$, as confirmed by our test measurements with various thicknesses. Fig. 4a–c present the R_{xy} vs. J loops measured at 275 K of Fe_3GaTe_2 (18.3 nm)/Pt (5.0 nm), Fe_3GaTe_2 (16.7 nm)/Pt (2.0 nm)/Ti (10.0 nm), and Fe_3GaTe_2 (15.8 nm)/Ti (10.0 nm) Hall bar devices. Deterministic magnetization switching was observed in all devices, with $J_{switching}$ estimated to be approximately $9.2 \times 10^6 \text{ A/cm}^2$, $5.9 \times 10^6 \text{ A/cm}^2$, and $2.4 \times 10^6 \text{ A/cm}^2$ for the respective devices. Notably, the $J_{switching}$ of the Fe_3GaTe_2 (15.8 nm)/Ti (10.0 nm) device is about four times smaller

than that of the Fe_3GaTe_2 (18.3 nm)/Pt (5.0 nm) device, suggesting that the OT efficiency in the $\text{Fe}_3\text{GaTe}_2/\text{Ti}$ heterostructure is higher than the SOT efficiency in the $\text{Fe}_3\text{GaTe}_2/\text{Pt}$ heterostructure. For the combined OT and SOT effect, the $J_{switching}$ ($5.9 \times 10^6 \text{ A/cm}^2$) is higher than in the OT-only $\text{Fe}_3\text{GaTe}_2/\text{Ti}$ device but lower than in the SOT-only $\text{Fe}_3\text{GaTe}_2/\text{Pt}$ device. In addition, during current-induced orbital/spin torque magnetization switching measurements, the testing connection is $I^+ - V^- - I^- - V^+$ for the $\text{Fe}_3\text{GaTe}_2/\text{Pt}$ device and $I^+ - V^+ - I^- - V^-$ for $\text{Fe}_3\text{GaTe}_2/\text{Pt}/\text{Ti}$ and $\text{Fe}_3\text{GaTe}_2/\text{Ti}$ devices along the clockwise direction. In this case, although the R_{xy} vs. J loops present the same polarity shown in Fig. 4a–c, the OT- and SOT-driven magnetization switching has the opposite polarity due to the different testing connection, which further

confirms the OHE of the Ti OHM in the $\text{Fe}_3\text{GaTe}_2/\text{Ti}$ heterostructure and the SHE of the Pt SHM in the $\text{Fe}_3\text{GaTe}_2/\text{Pt}$ heterostructure.

Figure 4d illustrates the possible physical mechanism behind the magnetization switching of these devices with different switching efficiency. For the $\text{Fe}_3\text{GaTe}_2/\text{Pt}$ device, the J_C directly converts into the J_S in the Pt layer, the switching efficiency mainly depends on the SOT from the Pt SHM ($\sigma_{\text{SHE,Pt}}$), as shown in the left panel of Fig. 4d. However, for the $\text{Fe}_3\text{GaTe}_2/\text{Ti}$ device, the switching efficiency is primarily influenced by both the OT of the Ti OHM ($\sigma_{\text{OHE,Ti}}$) and the spin-orbital correlation strength of the 2D-vdW FM Fe_3GaTe_2 layer. The J_C first converts into the J_L in the Ti layer, and then the J_L is converted into the J_S via the 2D-vdW FM Fe_3GaTe_2 layer, as presented in the right panel of Fig. 4. Considering the large OHE of the Ti, the significantly lower $J_{\text{switching}}$ of the $\text{Fe}_3\text{GaTe}_2/\text{Ti}$ device compared to that of the $\text{Fe}_3\text{GaTe}_2/\text{Pt}$ device indicates a rather strong spin-orbit correlation within the 2D-vdW FM Fe_3GaTe_2 layer. For the $\text{Fe}_3\text{GaTe}_2/\text{Pt}/\text{Ti}$ device, the Pt SHM serves as an SOT source, and the Ti OHM acts as an OT source. The J_S originates from two mechanisms: the J_C -to- J_S conversion through the Pt SHM and the J_C -to- J_L -to- J_S conversion through the Ti OHM and the 2D-vdW FM Fe_3GaTe_2 layer. During this process, the Pt SHM converts not only the J_C into the J_S but also some of the J_L from the Ti OHM into the J_S ^{42,44}. The rest of J_L from the Ti OHM may pass through the Pt layer and flow into the 2D-vdW FM Fe_3GaTe_2 layer, and then be converted into J_S . The Pt layer may partially screen the J_L flowing from the Ti OHM into the 2D-vdW FM Fe_3GaTe_2 layer, which diminishes the OT switching efficiency compared to that of the pure OT device, $\text{Fe}_3\text{GaTe}_2/\text{Ti}$. As a result, the $J_{\text{switching}}$ ($-5.9 \times 10^6 \text{ A/cm}^2$) of the $\text{Fe}_3\text{GaTe}_2/\text{Pt}/\text{Ti}$ device falls between the values observed for the $\text{Fe}_3\text{GaTe}_2/\text{Ti}$ and the $\text{Fe}_3\text{GaTe}_2/\text{Pt}$ devices. We also summarize the $J_{\text{switching}}$ as a function of the in-plane H_{ext} for the 2D-vdW FM Fe_3GaTe_2 devices measured at room temperature switched by the different SHMs and OHMs, as plotted in Fig. 4e. Very interestingly, the $J_{\text{switching}}$ of the Fe_3GaTe_2 devices switched via the light material Ti through OT is comparable to that of the Fe_3GaTe_2 devices driven by topological quantum materials through SOT [e.g., $\text{Bi}_{1.1}\text{Sb}_{0.9}\text{Te}_2\text{S}_1$ ³⁷, TalrTe_4 ³⁸, and WTe_2 ³⁹]. This finding highlights the highly efficient conversion process of J_C -to- J_L -to- J_S in the 2D-vdW FM Fe_3GaTe_2 layer, with potential implications for other 2D-vdW ferromagnets.

Spin-orbit correlation in the vdW ferromagnet

Based on the experimental results, we demonstrated that the $\text{Fe}_3\text{GaTe}_2/\text{Ti}$ device exhibits high OT efficiency, as evidenced by its low J_S , which arises from the contribution of both the Ti OHM and the 2D-vdW FM Fe_3GaTe_2 layer. The σ_{OHE} of the Ti OHM has been calculated to be $\sim 4600 (\hbar/e)(\text{S/cm})$ (see Fig. 1b), making it one of the highest among OHMs. The $\eta_{L,S}$, which represents the strength of spin-orbit correlation ($L \cdot S$) in 2D-vdW ferromagnets, is also expected to be significantly stronger. To verify this unique characteristic of the Fe_3GaTe_2 , we chose the monolayer, bilayer, trilayer, and bulk structures for theoretical calculations, as shown in Fig. 5a. Comprehensive electronic simulations based on density functional theory were then performed to determine their spin-orbit correlation functions (see calculation details in the Methods and Supplementary Note 4). The FM ground state of the Fe_3GaTe_2 was adopted in calculations for all the structures. For the monolayer Fe_3GaTe_2 , the magnetic moments are mainly located on the Fe-I ($-2.38 \mu_B$) and Fe-II atoms ($-1.41 \mu_B$), with small opposite contributions from Ga ($\sim -0.11 \mu_B$) and Te atoms ($\sim -0.09 \mu_B$) due to hybridization. Similarly, the bilayer, trilayer, and bulk Fe_3GaTe_2 exhibit a nearly identical distribution of magnetic moments as the monolayer Fe_3GaTe_2 , due to the relatively weak vdW interaction between the layers. Further analysis of the orbital resolved band structure reveals that the majority of electronic states near the Fermi level (E_F) are predominantly contributed by the $3d$ orbitals of Fe atoms, as illustrated in Fig. 5b for the monolayer Fe_3GaTe_2 . The orbital-projected band structure of monolayer Fe_3GaTe_2 structure with different d states of Fe is highlighted by different colors when SOC is considered.

The spin-orbit correlation ($L \cdot S$) of the FM materials describes the conversion efficiency between the orbital (L) and the spin (S). Therefore, we calculated the band-resolved spin-orbit correlation function $\langle L \cdot S \rangle_{k,n}$ ^{9,45} and its integrated value, i.e., spin-orbit correlation coefficient $\eta_{L,S} = \sum_n \int f_{k,n} \langle L \cdot S \rangle_{k,n} dV_{k,n}$ after constructing the effective Hamiltonian using the Wannier90 package^{46,47} (see Supplementary Note 4), where $f_{k,n} = f(\varepsilon_{k,n})$ represents the Fermi-Dirac distribution of the n th band, and $dV_{k,n}$ denotes the momentum-space volume element, which takes a uniform Brillouin zone sampling. The calculated results of $\langle L \cdot S \rangle_{k,n}$ are summarized in Fig. 5c-f, in which red and blue colored areas denote strong positive and negative correlations, respectively. The positive value means that orbital angular momentum is converted to spin angular momentum in the same direction, and vice versa⁴⁸. It is evident that positive/negative correlation hotspots appear near the E_F (e.g., around the K and $K\bar{I}$ points) corresponding to strong orbital-to-spin conversion efficiency. Further orbital analysis around these hotspots shows a significant hybridization of the $3d$ orbitals (d_{xy} , $d_{x^2-y^2}$, d_{z^2}), which leads to the large spin-orbit correlation, as shown in Fig. 5b ($L \cdot S$). This is because the wave function that consists of d_{xy} and $d_{x^2-y^2}$ gives a larger matrix element's value of the SOC operator $L \cdot S$ ⁴⁹. Note that these spin-orbit correlation hotspots occur in only one spin channel, which may further enhance the orbital-to-spin conversion during the OT switching process. Similar correlation hotspots can be observed for bilayer, trilayer, and bulk Fe_3GaTe_2 structures near the E_F (especially near the K and $K\bar{I}$ points), as plotted in Fig. 5d-f, confirming the robust spin-orbit correlation in Fe_3GaTe_2 .

The spin-orbit correlation coefficient $\eta_{L,S}$ was calculated to be around 0.375, 0.755, 1.153, and 0.762 for the monolayer, bilayer, trilayer, and bulk Fe_3GaTe_2 structures, respectively. The bulk Fe_3GaTe_2 structure contains two layers in the unit cell that are the same as the bilayer structure, leading to comparable $\eta_{L,S}$ values between bulk and bilayer systems. This variation of $\eta_{L,S}$ is due to the increased energy bands that contribute the $\langle L \cdot S \rangle_{k,n}$ below the E_F as the number of layers increases. Therefore, to compare the effective orbital-to-spin conversion efficiency in the monolayer, bilayer, trilayer, and bulk Fe_3GaTe_2 structures, we defined $\eta_{L,S}^{\text{eff}} = \eta_{L,S}/N$ (N is the number of layers) to assess the spin-orbit correlation of each layer, which was estimated to be around 0.3752, 0.3773, 0.3842, and 0.3809, respectively, almost independent of the layer thickness. It is important to note that the 2D-vdW PMA ferromagnets are fundamentally different from traditional bulk PMA FM material due to their unique 2D-vdW nature. The switching of each magnetic layer could be much easier because of the robust thickness-independent $\eta_{L,S}^{\text{eff}}$ and the rather weak interlayer coupling. While $\eta_{L,S}/N$ is layer-independent in our model, practical efficiency is limited by the λ_{OHE} , beyond which additional layers do not contribute significantly. These results not only reveal the different J_L -to- J_S conversion mechanisms between the 2D-vdW ferromagnets and traditional ferromagnets but also provide insight into understanding the J_L transport in the ferromagnets with unique 2D-vdW features.

Discussion

To summarize, we investigated the current-induced magnetization switching of the 2D-vdW FM Fe_3GaTe_2 heterostructures using Ti, Pt, and Pt/Ti. We found that the OT from the Ti OHM enables efficient magnetization switching of the 2D-vdW FM Fe_3GaTe_2 at 275 K with the $J_{\text{switching}} \sim 2.4 \times 10^6 \text{ A/cm}^2$, compared to the SOT from the Pt ($J_{\text{switching}} \sim 9.2 \times 10^6 \text{ A/cm}^2$) and the combined SOT+OT from the Pt/Ti ($J_{\text{switching}} \sim 5.9 \times 10^6 \text{ A/cm}^2$). This indicates a highly efficient J_C -to- J_L -to- J_S conversion in the 2D-vdW $\text{Fe}_3\text{GaTe}_2/\text{Ti}$ heterostructure. The underlying physical mechanism is that the Ti OHM efficiently converts the J_C into the J_L due to its high $\sigma_{\text{OHE}} \sim 4600 (\hbar/e)(\text{S/cm})$, while the Fe_3GaTe_2 effectively converts the J_L into the J_S via a significant and layer-independent $\eta_{L,S}$, as confirmed by the spin-orbit correlation calculations.

The efficient 2D-vdW orbitronic devices can be realized through the optimal selection of the OHMs and the 2D-vdW ferromagnet to

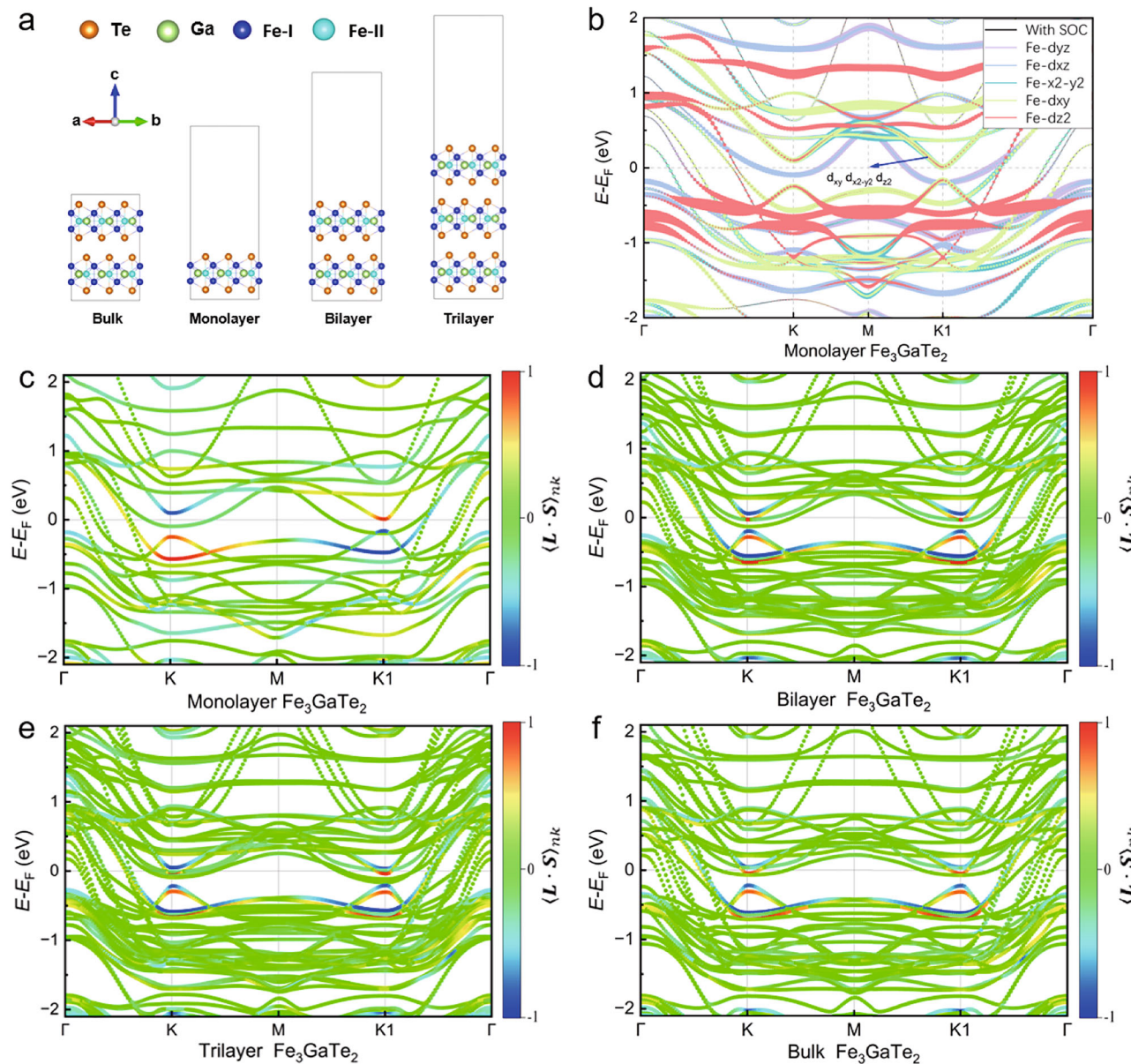


Fig. 5 | Theoretical calculation of spin-orbit correlation function ($L \cdot S$)_{nk}. **a** The monolayer, bilayer, trilayer, and bulk Fe_3GaTe_2 structures, in which the Fe-I, Fe-II, Ga, and Te atoms are colored blue, light blue, green, and orange, respectively. **b** The orbital-projected band structure of monolayer Fe_3GaTe_2 structure with different d states of Fe is highlighted by different colors. **c–f** The calculated band-resolved

spin-orbit correlation function $\langle L \cdot S \rangle_{nk}$ of the monolayer, bilayer, trilayer, and bulk Fe_3GaTe_2 structures, respectively. The color represents the correlation for each eigenstate, in which red and blue denote strong positive and negative correlations, respectively. Note that the Fermi energy is set to zero for reference.

obtain the efficient conversion of the J_C -to- J_L -to- J_S . Most importantly, investigating the conversion process and transport properties of the J_L in the 2D-vdW FM Fe_3GaTe_2 is crucial for understanding the physical mechanisms behind the J_L -to- J_S conversion and magnetization switching in 2D-vdW FM OT heterostructures. In addition, because of the weak interlayer coupling, 2D-vdW FM materials may lead to much faster magnetization switching of each FM layer. Our experimental and theoretical findings carry important implications for the development of efficient 2D-vdW orbitronic memory and logic devices.

Methods

Crystal growth and property characterizations

High-quality Fe_3GaTe_2 single crystal samples were grown by the self-flux method. Tellurium (Te) powder (99.999%), gallium (Ga) balls (99.9999%), and iron (Fe) powder (99.95%) in a molar ratio of 2:1:2 were

sealed in an evacuated quartz tube using a hydrogen-oxygen cutting machine. Subsequently, the quartz tube was heated from room temperature to 1000 °C for 60 min in a muffle furnace and maintained at 1000 °C for 1440 min, then cooled down from 1000 °C to 780 °C with three-temperature steps. After that, the quartz tube was quenched in the ice water. The crystalline and magnetic properties of the Fe_3GaTe_2 flakes were characterized by powder X-ray diffraction (XRD), scanning transmission electron microscopy (STEM), physical property measurement system (PPMS), and vibrating sample magnetometer (Model 3107, East Changing Technologies, China).

Device fabrication and transport-property measurements

2D-vdW FM $\text{Fe}_3\text{GaTe}_2/X$ ($X = \text{Ti}$, Pt , and Pt/Ti) Hall bar devices were prepared by combining mechanical exfoliation and magnetron sputtering. 2D-vdW FM Fe_3GaTe_2 layers were exfoliated on Si/SiO_2

substrates in an Argon-filled glove box and then transferred into the chamber of the sputtering system with a base pressure lower than 5.0×10^{-8} Torr. After slight surface cleaning, the Ti, Pt, and Pt/Ti layers were deposited on the Fe_3GaTe_2 layer capped with a 3.0 nm-thick SiO_2 layer. During the deposition process, the Ar working pressure is 3.0 mTorr. Subsequently, the $\text{Fe}_3\text{GaTe}_2/\text{Ti}$, $\text{Fe}_3\text{GaTe}_2/\text{Pt}/\text{Ti}$, and $\text{Fe}_3\text{GaTe}_2/\text{Pt}$ samples were patterned into 4-terminal Hall bar devices through the standard photolithography and an Ar ion milling technique.

In the ST-FMR measurements, the RF signals with frequencies from 8.5 to 10.5 GHz were applied along the longitudinal axis using a high-frequency signal generator, delivering a nominal maximum power of -23 dBm. Angular-dependent measurements were performed by sweeping the in-plane H_{ext} while systematically varying the azimuthal angle φ between the H_{ext} and the longitudinal axis (\hat{x}). Because the highest signal/noise ratio was obtained at 6.0–8.5 GHz, 8.5 GHz was usually chosen for angular-dependent $V_{\text{mix}}(H, \varphi)$ scanning. The experimental configuration enables quantitative extraction of both orbital torque efficiency through rigorous analysis of the ST-FMR linewidth and mixing voltage amplitude angular dependence.

The in-plane harmonic Hall voltage measurements were performed using an alternating current to evaluate the orbit torque of the $\text{Fe}_3\text{GaTe}_2/\text{Ti}$ heterostructures. The samples were fixed on a rotating rod, and a constant H_{ext} was applied. The rotating rod was controlled by a motor to allow the sample to rotate in-plane, thereby changing the angle (azimuth φ) between the H_{ext} and the current direction. The Hall voltage response was measured at both the first V_{xy}^{ω} and second $V_{xy}^{2\omega}$ harmonic frequencies. A current of 0.75 mA was applied for the Fe_3GaTe_2 (-15 nm)/Ti (10 nm) device to stimulate the orbit torque and Hall signal. The current was supplied using a Keithley 6221 current source. Both V_{xy}^{ω} and $V_{xy}^{2\omega}$ were recorded by two SR830 DSP lock-in amplifiers at the same time while varying the azimuthal angle (φ) under a constant H_{ext} .

The anomalous Hall resistance (R_{AHE}) vs. H_{ext} loops of the $\text{Fe}_3\text{GaTe}_2/\text{Ti}$, $\text{Fe}_3\text{GaTe}_2/\text{Pt}/\text{Ti}$, and $\text{Fe}_3\text{GaTe}_2/\text{Pt}$ Hall bar devices were measured using the Electrical Transport Option of the PPMS Dynacool system. Current-induced magnetization switching experiments were performed with a fixed in-plane H_{ext} of ± 20 mT - ± 150 mT along the current direction by interfacing a Keithley 6221 current source and 2182 A nanovoltmeter in the Multi-Field Technology Company system. The testing connection for $\text{Fe}_3\text{GaTe}_2/\text{Ti}$ and $\text{Fe}_3\text{GaTe}_2/\text{Pt}/\text{Ti}$ devices is $I^+ - V^+ - I^- - V^-$ along the clockwise direction compared to the normal testing connection ($I^+ - V^- - I^- - V^+$) for the $\text{Fe}_3\text{GaTe}_2/\text{Pt}$ device.

Theoretical calculation

Bulk vdW FM Fe_3GaTe_2 shares hexagonal structure with space group $P6_3/\text{mmc}$ ($a = b = 3.986$ Å, $c = 16.229$ Å, $\alpha = \beta = 90^\circ$, $\gamma = 120^\circ$). In each Fe_3GaTe_2 layer, the Fe_3Ga heterometallic slab is sandwiched between two Te layers, as illustrated in Fig. 1a. To eliminate interactions between slabs along the z direction, we adopted 20 Å vacuum layer along the z-axis. The adjacent slabs were connected by weak vdW forces with an interlayer spacing of 0.81 nm. We performed first-principles calculations based on the density functional theory (DFT) as implemented in the Vienna ab initio simulation package (VASP)^{50,51}, which is treated by the projector-augmented plane-wave (PAW) method and utilized a plane wave basis set⁵². The exchange-correlation potential terms were considered at the level of generalized gradient approximation (GGA) within the scheme of Perdew-Burke-Ernzerhof (PBE) functional⁵³. For few-layer and bulk structures, the long-range vdW interactions [DFT-D3 method⁵⁴] were incorporated to correct its total energy. The plane-wave cutoff energy is chosen as 400 eV, and we sample the Brillouin zone on $15 \times 15 \times 1$ and $15 \times 15 \times 3$ regular mesh for the self-consistent calculations of few-layer and bulk Fe_3GaTe_2 structures, respectively. Layer number N refers to the count of Te-Fe-Ga-Fe-Te structural units in the simulated supercell. The geometric optimizations were performed with a convergence criterion of 10^{-5} eV.

Data availability

The authors declare that the data supporting the findings of this study are available within the main text and Supplementary Information files.

References

1. Dieny, B. et al. Opportunities and challenges for spintronics in the microelectronics industry. *Nat. Electron.* **3**, 446–459 (2020).
2. Shao, Q. et al. Roadmap of spin-orbit torques. *IEEE Trans. Magn.* **57**, 800439 (2021).
3. Guo, Z. X. et al. Spintronics for energy efficient computing: an overview and outlook. *Proc. IEEE* **109**, 1398–1417 (2021).
4. Brataas, A., Kent, A. D. & Ohno, H. Current-induced torques in magnetic materials. *Nat. Mater.* **11**, 372–381 (2012).
5. Liu, L. et al. Spin-torque switching with the giant spin Hall effect of tantalum. *Science* **336**, 555–558 (2012).
6. Sinova, J. et al. Spin Hall effects. *Rev. Mod. Phys.* **87**, 1213 (2015).
7. Song, C. et al. Spin-orbit torques: Materials, mechanisms, performances, and potential applications. *Prog. Mater. Sci.* **118**, 100761 (2021).
8. Bernevig, B. A., Hughes, T. L. & Zhang, S. C. Orbitronics: the intrinsic orbital current in p-doped silicon. *Phys. Rev. Lett.* **95**, 066601 (2005).
9. Kontani, H. et al. Giant orbital Hall effect in transition metals: origin of large spin and anomalous Hall effects. *Phys. Rev. Lett.* **102**, 016601 (2009).
10. Go, D. et al. Intrinsic spin and orbital Hall effects from orbital texture. *Phys. Rev. Lett.* **121**, 086602 (2018).
11. Jo, D., Go, D. & Lee, H.-W. Gigantic intrinsic orbital Hall effects in weakly spin-orbit coupled metals. *Phys. Rev. B* **98**, 214405 (2018).
12. Lee, D. et al. Orbital torque in magnetic bilayers. *Nat. Commun.* **12**, 6710 (2021).
13. Han, S., Lee, H. W. & Kim, K. W. Orbital dynamics in centrosymmetric systems. *Phys. Rev. Lett.* **128**, 176601 (2022).
14. Sala, G. & Gambardella, P. Giant orbital Hall effect and orbital-to-spin conversion in 3d, 5d, and 4f metallic heterostructures. *Phys. Rev. Res.* **4**, 033037 (2022).
15. Go, D. et al. Long-range orbital torque by momentum-space hot-spots. *Phys. Rev. Lett.* **130**, 246701 (2023).
16. Choi, Y. G. et al. Observation of the orbital Hall effect in a light metal Ti. *Nature* **619**, 52–56 (2023).
17. Hayashi, H. et al. Observation of long-range orbital transport and giant orbital torque. *Commun. Phys.* **6**, 32 (2023).
18. Sala, G. et al. Orbital Hanle magnetoresistance in a 3d transition metal. *Phys. Rev. Lett.* **131**, 156703 (2023).
19. Hayashi, H. et al. Observation of orbital pumping. *Nat. Electron.* **7**, 646–652 (2024).
20. Yang, Y. H. et al. Orbital torque switching in perpendicularly magnetized materials. *Nat. Commun.* **15**, 8645 (2024).
21. Xie, H. et al. Efficient noncollinear antiferromagnetic state switching induced by the orbital Hall effect in chromium. *Nano Lett.* **23**, 10274–10281 (2023).
22. Zheng, Z. et al. Effective electrical manipulation of a topological antiferromagnet by orbital torques. *Nat. Commun.* **15**, 745 (2024).
23. Lee, H. & Lee, H.-W. Composition dependence of the orbital torque in $\text{Co}_x\text{Fe}_{1-x}$ and $\text{Ni}_x\text{Fe}_{1-x}$ alloys: Spin-orbit correlation analysis. *Curr. Appl. Phys.* **67**, 60–68 (2024).
24. Gong, C. et al. Discovery of intrinsic ferromagnetism in two-dimensional van der Waals crystals. *Nature* **546**, 265–269 (2017).
25. Huang, B. et al. Layer-dependent ferromagnetism in a van der Waals crystal down to the monolayer limit. *Nature* **546**, 270–273 (2017).
26. Lin, X. et al. Two-dimensional spintronics for low-power electronics. *Nat. Electron.* **2**, 274–283 (2019).
27. Yang, H. et al. Two-dimensional materials prospects for non-volatile spintronic memories. *Nature* **606**, 663–673 (2022).

28. Zhu, W. et al. Large room-temperature magnetoresistance in van der Waals ferromagnet/semiconductor junctions. *Chin. Phys. Lett.* **39**, 128501 (2022).
29. Pan, Z.-C. et al. Room-temperature orbit-transfer torque enabling van der Waals magnetoresistive memories. *Sci. Bull.* **68**, 2743–2749 (2023).
30. Li, Z. et al. Room-temperature sub-100 nm Néel-type skyrmions in non-stoichiometric van der Waals ferromagnet $\text{Fe}_{3-x}\text{GaTe}_2$ with ultrafast laser writability. *Nat. Commun.* **15**, 1017 (2024).
31. Lv, X. et al. Distinct skyrmion phases at room temperature in two-dimensional ferromagnet Fe_3GaTe_2 . *Nat. Commun.* **15**, 3278 (2024).
32. Zhang, C. et al. Above-room-temperature chiral skyrmion lattice and Dzyaloshinskii-Moriya interaction in a van der Waals ferromagnet $\text{Fe}_{3-x}\text{GaTe}_2$. *Nat. Commun.* **15**, 4472 (2024).
33. Liu, C. et al. Magnetic skyrmions above room temperature in a van der Waals ferromagnet Fe_3GaTe_2 . *Adv. Mater.* **36**, 2311022 (2024).
34. Li, W. H. et al. Room-temperature van der Waals ferromagnet switching by spin-orbit torques. *Adv. Mater.* **35**, 2303688 (2023).
35. Yun, C. et al. Efficient current-induced spin torques and field-free magnetization switching in a room-temperature van der Waals magnet. *Sci. Adv.* **9**, eadj3955 (2023).
36. Kajale, S. N. et al. Current-induced switching of a van der Waals ferromagnet at room temperature. *Nat. Commun.* **15**, 1485 (2024).
37. Choi, G. S. et al. Highly efficient room-temperature spin-orbit-torque switching in a Van der Waals heterostructure of topological insulator and ferromagnet. *Adv. Sci.* **11**, 2400893 (2024).
38. Zhang, Y. et al. Robust field-free switching using large unconventional spin-orbit torque in an all-Van der Waals heterostructure. *Adv. Mater.* **36**, 2406464 (2024).
39. Kajale, S. N. et al. Field-free deterministic switching of all-van der Waals spin-orbit torque system above room temperature. *Sci. Adv.* **10**, eadk8669 (2024).
40. Zhang, G. et al. Above-room-temperature strong intrinsic ferromagnetism in 2D van der Waals Fe_3GaTe_2 with large perpendicular magnetic anisotropy. *Nat. Commun.* **13**, 5067 (2022).
41. Xu, H. et al. High spin Hall conductivity in large-area type-II Dirac semimetal PtTe_2 . *Adv. Mater.* **32**, 2000513 (2020).
42. Lee, S. et al. Efficient conversion of orbital Hall current to spin current for spin-orbit torque switching. *Commun. Phys.* **4**, 234 (2021).
43. Gao, T. H. et al. Control of dynamic orbital response in ferromagnets via crystal symmetry. *Nat. Phys.* **20**, 1896–1903 (2024).
44. Ding, S. L. et al. Harnessing orbital-to-spin conversion of interfacial orbital currents for efficient spin-orbit torques. *Phys. Rev. Lett.* **125**, 177201 (2020).
45. Tanaka, T. et al. Intrinsic spin Hall effect and orbital Hall effect in 4d and 5d transition metals. *Phys. Rev. B* **77**, 165117 (2008).
46. Souza, I., Marzari, N. & Vanderbilt, D. Maximally localized Wannier functions for entangled energy bands. *Phys. Rev. B* **65**, 035109 (2001).
47. Marzari, N. & Vanderbilt, D. Maximally localized generalized Wannier functions for composite energy bands. *Phys. Rev. B* **56**, 12847 (1997).
48. Schreier, M. et al. Sign of inverse spin Hall voltages generated by ferromagnetic resonance and temperature gradients in yttrium iron garnet platinum bilayers. *J. Phys. D Appl. Phys.* **48**, 025001 (2015).
49. Konschuh, S., Gmitra, M. & Fabian, J. Tight-binding theory of the spin-orbit coupling in grapheme. *Phys. Rev. B* **82**, 245412 (2010).
50. Kresse, G. & Furthmüller, J. Efficiency of ab-initio total energy calculations for metals and semiconductors using a plane-wave basis set. *Comput. Mater. Sci.* **6**, 15 (1996).
51. Kresse, G. & Hafner, J. Ab initio molecular-dynamics simulation of the liquid-metal-amorphous-semiconductor transition in Germanium. *Phys. Rev. B* **49**, 14251 (1994).
52. Blöchl, P. E. Projector augmented-wave method. *Phys. Rev. B* **50**, 17953 (1994).
53. Perdew, J. P. et al. Atoms, molecules, solids, and surfaces: applications of the generalized gradient approximation for exchange and correlation. *Phys. Rev. B* **46**, 6671 (1992).
54. Grimme, S. Semiempirical GGA-type density functional constructed with a long-range dispersion correction. *J. Comput. Chem.* **27**, 1787 (2006).

Acknowledgements

This work was supported by the National Key R&D Program of China [2022YFA1204003 (Y.J.)], the National Natural Science Foundation of China [Grant Nos. U24A6002 (Y.J.), 52271240 (D.L.Z.), U23A20551 (D.L.Z.), 12204037 (W.J.), 12474121 (L.L.)], the Key project of the Natural Science Foundation of Tianjin [Grant No. 23JCZDJC00400 (D.L.Z.)], and the Ministry of Science and Technology of China [Grant No. 2024YFA1410100 (L.L.)]. D.L.Z. gratefully acknowledges the research funding provided by the Cangzhou Institute of Tiangong University [Grant No. TGCYY-F-0201 (D.L.Z.)], the Key R&D Program of Cangzhou [222104008 (D.L.Z.)], and the Open Fund of the State Key Laboratory of Spintronics Devices and Technologies [Grants No. SPL-2402 (D.L.Z.)]. We would like to thank the Analytical & Testing Center of Tiangong University.

Author contributions

D.L.Z., H.S.W., J.Y.D., and J.L.C. contributed equally to this work. D.L.Z conceived the work and designed all the samples. Y.J. coordinated and supervised the project. H.S.W. and J.Y.D. prepared the samples and patterned the Hall bar devices with the help by Y.H.Y. and J.L.G.. J.Y.D. and H.S.W. carried out the ST-FMR measurement, and current-induced orbital/spin-torque magnetization switching experiments with the help P.W., P.F.L., S.H., and Z.Y.J.. J.L.C., and W.J. performed the first-principles calculations. D.D.Y., J.X.Y., and K.Z. prepared the Fe_3GaTe_2 single crystals and characterized the crystalline structure and magnetic properties. J.X.C., W.X.G., and L.L. carried out the harmonic Hall voltage measurements. W.H.W. and Y.L. help testing and analyzing the experimental data. D.L.Z. and W.J. wrote the manuscript with inputs from all the authors. All the authors discussed the results and commented on the manuscript.

Competing interests

The authors declare no competing interests.

Additional information

Supplementary information The online version contains supplementary material available at <https://doi.org/10.1038/s41467-025-62333-5>.

Correspondence and requests for materials should be addressed to Delin Zhang, Wei Jiang or Yong Jiang.

Peer review information *Nature Communications* thanks the anonymous reviewers for their contribution to the peer review of this work. A peer review file is available.

Reprints and permissions information is available at <http://www.nature.com/reprints>

Publisher's note Springer Nature remains neutral with regard to jurisdictional claims in published maps and institutional affiliations.

Open Access This article is licensed under a Creative Commons Attribution-NonCommercial-NoDerivatives 4.0 International License, which permits any non-commercial use, sharing, distribution and reproduction in any medium or format, as long as you give appropriate credit to the original author(s) and the source, provide a link to the Creative Commons licence, and indicate if you modified the licensed material. You do not have permission under this licence to share adapted material derived from this article or parts of it. The images or other third party material in this article are included in the article's Creative Commons licence, unless indicated otherwise in a credit line to the material. If material is not included in the article's Creative Commons licence and your intended use is not permitted by statutory regulation or exceeds the permitted use, you will need to obtain permission directly from the copyright holder. To view a copy of this licence, visit <http://creativecommons.org/licenses/by-nc-nd/4.0/>.

© The Author(s) 2025